

UCSF

UC San Francisco Previously Published Works

Title

Evaluation of pressure-driven brain infusions in nonhuman primates by intra-operative 7 tesla MRI

Permalink

<https://escholarship.org/uc/item/84f5616v>

Journal

Journal of Magnetic Resonance Imaging, 36(6)

ISSN

1053-1807

Authors

Rosenbluth, Kathryn H
Martin, Alastair J
Bringas, John
[et al.](#)

Publication Date

2012-12-01

DOI

10.1002/jmri.23771

Peer reviewed



Published in final edited form as:

J Magn Reson Imaging. 2012 December ; 36(6): 1339–1346. doi:10.1002/jmri.23771.

Evaluation of pressure-driven brain infusions in non-human primates by intra-operative 7 Tesla MRI

Kathryn H. Rosenbluth, PhD¹, Alastair J. Martin, PhD², John Bringas, MS¹, and Krystof S. Bankiewicz, MD PhD¹

¹Department of Neurosurgery, University of California San Francisco (UCSF), San Francisco, CA USA

²Department of Radiology and Biomedical Imaging, UCSF

Abstract

PURPOSE—The goal of this study was to characterize the effects of pressure-driven brain infusions using high field intra-operative MRI. Understanding these effects is critical for upcoming neurodegeneration and oncology trials using convection-enhanced delivery (CED) to achieve large drug distributions with minimal off-target exposure.

MATERIALS AND METHODS—High-resolution T2-weighted and diffusion-tensor images were acquired serially on a 7 Tesla MRI scanner during six CED infusions in non-human primates. The images were used to evaluate the size, distribution, diffusivity and temporal dynamics of the infusions.

RESULTS—The infusion distribution had high contrast in the T2-weighted images. Diffusion tensor images showed the infusion increased diffusivity, reduced tortuosity and reduced anisotropy. These results suggested CED caused an increase in the extracellular space.

CONCLUSIONS—High-field intra-operative MRI can be used to monitor the distribution of infusate and changes in the geometry of the brain's porous matrix. These techniques could be used to optimize the effectiveness of pressure-driven drug delivery to the brain.

Keywords

7T MRI; convection-enhanced drug delivery; diffusion; extracellular space; non-human primate

INTRODUCTION

Convection enhanced delivery (CED) is a technique that uses pressure-driven infusions from cannulae in the brain to achieve large local drug distributions (1). CED is advantageous to systemic drug delivery because it bypasses the blood-brain barrier and is preferable to diffusion-driven methods because it distributes drugs to larger volumes of tissue. CED is an especially promising technology for large therapeutics with stringent requirements to minimize off-target exposure, including chemotherapy drugs for brain tumors (2) and gene therapy treatments for neurodegenerative disorders (3–5).

Understanding the exact distribution of infusate in CED infusions and the changes in the geometry of the brain's porous matrix within the infusions is important for optimizing the distribution of drugs in the brain. Previous studies at 1.5T and 3T have shown that T2-

hyperintensity accurately reflects the CED distribution as measured by gadolinium-enhanced T1-hyperintensity (6), SPECT imaging (7) and protein expression following gene therapy (6).

Performing this study at 7T permitted rapid acquisition of serial T2-weighted images to capture the temporal dynamics of the infusion with an in-plane resolution below 0.25mm. The high signal was especially important for this study because of the relatively small size of primate brains, which are about 12 times smaller by volume than human brains. Diffusion-tensor images (DTI) were also serially acquired to measure changes in the geometry of the fluid pathways. The temporal resolution for acquiring both the T2-weighted and DTI images was below 8 minutes. DTI has previously been used to estimate brain geometry for surgical planning algorithms (8–10). Diffusion provides relevant information on changes in the matrix structure because diffusivity and anisotropy reflect the same pore geometry of the matrix that determines the hydraulic conductivity in CED.

This study had two goals: first, to establish clinically feasible methods for using intraoperative high field MRI to accurately characterize the distribution of infusate and investigate changes in the porous extracellular matrix of mammalian brain during CED and, second, to estimate the expansion of the extracellular space. Serial high-resolution images of infusions in non-human primates (NHP) were acquired intra-operatively in a 7T MRI scanner. These images were used to measure the size, diffusivity, anisotropy and temporal dynamics of the infusate distribution in the porous extracellular matrix. The results and methodologies developed in this study are relevant to upcoming trials of emerging therapeutic agents, including macromolecules, viral particles, liposomal constructs and even potentially cells.

METHODS

Image Acquisition and Processing

Six saline CED infusions in rhesus monkeys (*Macaca mulata*) were performed intra-operatively in the MRI scanner. The study was approved by the Institutional Animal Care and Use Committee at our institution. The animals were imaged in supine position in a whole-body 7T MRI scanner (General Electric Healthcare, Milwaukee, WI) using a volume transmit RF coil with active detuning and an eight-channel phased array receive RF coil (Nova Medical, Wilmington, MA).

The MRI protocol began with a high-resolution Gradient Recalled Echo (GRE) to visualize the anatomy and plan the procedure. The GRE was acquired in 13 minutes with a matrix size of 512 by 512 over a 15cm field-of-view, 24 interleaved slices each 1.5mm thick, TE 12ms, TR 250ms, flip 20°, bandwidth 31.25kHz and 3 repetitions.

After beginning the infusion, alternating coronal T2-weighted and DTI images were acquired serially to measure the distribution of infusate and the changes in the tissue structure. The T2-weighted scan was a Fast Spin Echo (FSE) acquired in 4.3 minutes with a matrix size of 512 by 512 over a 12cm field-of-view, 18 interleaved slices each 2mm thick, TE 85ms, TR 3950ms, ETL 16, bandwidth 12.5 kHz, 1 repetition and phase encoding in the superior-inferior direction. The DTI scan was a single-shot spin echo echo-planar imaging acquisition that utilized novel radiofrequency pulses and eight-channel parallel imaging using SENSE with a factor of 2 to minimize distortion and acquisition time protocol (11). The DTI was acquired with 6 directions and a b-value of 400s/mm² to provide a fast acquisition with high sensitivity to increasing diffusion. The b-value is lower than the typical 800 to 1000s/mm² used to measure ischemic cellular swelling because the infusion was expected to increase rather than decrease diffusivity. The DTI was acquired in 3.5

minutes with a TE of 90.1ms, a TR of 5000ms, a matrix size of 128 by 128 with 2 repetitions, phase encoding in the superior-inferior direction, a field-of-view of 12cm and 25 interleaved slices each 2mm thick. Apparent Diffusion Coefficient (ADC) and Fractional Anisotropy (FA) were evaluated on a pixel-by-pixel basis using iPlan software (Brainlab, Munich). The high field strength posed a challenge for image distortion in the DTI due to the EPI-based acquisition and small size of the primate brain. DTI datasets were corrected for eddy currents and elastically fused to the undistorted T2-FSE images, also using iPlan software. Representative GRE, T2-FSE and DTI images are shown in Fig. 1 and Fig. 2.

Subjects and Infusion Method

The six CED infusions were bilateral infusions performed during three sessions. One NHP received bilateral saline infusions at Day 0 and Day 21, affording the opportunity to evaluate the tissue recovery from the first infusion. A second NHP received bilateral saline infusions only at Day 0.

The animal infusion protocol followed previously established methods (12). Each animal underwent neurosurgical procedures to bilaterally position threaded rings and plugs onto the skull approximately 2 weeks prior to the infusion. Immediately prior to imaging, the animals were sedated with ketamine (Ketaset, 7mg/kg, intramuscular) and xylazine (Rompum, 3mg/kg, intramuscular) and the plugs were replaced with threaded arrays. The holes of the array were filled with saline to make them visible on MRI and to prevent introduction of air. The animals were then intubated and placed on 1% to 3% inhaled isoflurane.

Each cannula consisted of two narrow fused silica tubes. The inner tube had an inner diameter of 150 μ m and an outer diameter of 350 μ m. The outer tube fit snugly around the inner tube and had an outer diameter of 450 μ m. The outer tube was 3mm shorter than the inner tube, providing a 3mm step from a diameter of 350 to 450 μ m to prevent reflux along the cannula tract (13). Each cannula was primed with saline and connected to an infusion line using a 20G Perifix catheter connector (B-Braun Inc., USA). Flow in the infusion line was driven by a 1mL Monoject syringe (Kendall Inc., USA) mounted onto an MRI-compatible infusion pump (Harvard Apparatus Inc., USA).

The GRE scan was acquired prior to inserting the cannulae to visualize the anatomy and to identify the optimal array hole for targeting the mid-thalamus. The thalamus was selected because its large size permitted large infusions without leakage into adjacent cerebrospinal fluid (CSF) spaces.

The animal was brought out from the bore and the cannula was slowly inserted through the array and into the brain to the target depth. Infusion flow was continuously maintained at 1 μ L/min during cannula insertion to prevent occlusion of the tip. The animal was returned to the isocenter of the MRI scanner for serial imaging of the infusion by T2-FSE and DTI. The rate of infusion was increased by 0.5 μ L/min every 5 minutes after the first appearance of infusate up to a maximum of 3 μ L/min. Each infusion lasted approximately 90 minutes and resulted in an infused volume of approximately 200 μ L.

Serial T2-weighted and DTI images were acquired for an additional 90 minutes after completion of each infusion to measure the tissue recovery. The high-resolution GRE was re-acquired at the end of each infusion and recovery period. The cannulae were then removed and the arrays were replaced with plug caps.

Image Analysis

Circular regions of interest (ROIs) 2.8mm in diameter were placed laterally to the cannula, as shown in Fig. 3. The ROIs were placed at least 1mm from the cannula to account for the

small fluid-filled cavity that develops around the tip (14). The average ADC and FA were measured in each ROI at each timepoint.

Tortuosity (τ) was calculated by comparing the restricted diffusion in the ROI to the free diffusion (ADC_0) in the ventricle (15,16):

$$\tau = \sqrt{\frac{ADC_0}{ADC_{ROI}}} \quad \text{Equation 1}$$

Tortuosity describes the restriction to diffusion resulting from the porous matrix formed by neural cells and vessels and has been validated by in-vivo iontophoresis (17).

The hyperintense region of the T2-FSE was outlined to evaluate the distribution volume (Vd) and the average changes in ADC and FA within this volume. Visual segmentation of the T2-hyperintensity has been previously shown to accurately depict the distribution of CED infusions (6,7). The infusion volume (Vi) was calculated by integrating the pump flow rate over the infusion time to define the Vd/Vi ratio. Vd/Vi is a standard metric describing the ratio of the volume of distribution in the brain (Vd) to the volume of infused fluid (Vi) (1). Vd is always larger than Vi because some space in the brain is taken up by cells and CED displaces only fluid in the extracellular space.

Porosity (θ) is the fractional volume of space occupied by extracellular fluid and was thus calculated as the inverse of the Vd/Vi ratio ($\theta = Vi/Vd$). The pore space around the cells and vessels in the brain is important to CED because it is the space through which the bulk flow of infusate occurs. The change in porosity was used to estimate the increase in hydraulic conductivity (k), which describes the flow velocity for the drug distribution by CED. Porosity and hydraulic conductivity are related by the Kozeny-Carman relation (18):

$$\frac{k}{k_0} = \left(\frac{\theta}{\theta_0}\right)^3 \left(\frac{1-\theta_0}{1-\theta}\right)^2 \quad \text{Equation 2}$$

The increase in hydraulic conductivity provided insight into the distribution of pore sizes. The hydraulic conductivity for a fluid-saturated porous medium with a small fluid volume fraction (19) is:

$$k \approx \frac{\xi^2}{\mu\theta^{1/3}} \quad \text{Equation 3}$$

where ξ is the pore size and μ is the viscosity of the interstitial fluid. The typical porosity of a healthy un-infused mammalian brain (θ_0) is about 20% (20–23). The fraction α of pores that selectively opened during the infusion was estimated by combining Eq. [2] and Eq. [3] and assuming the viscosity of the infusate is roughly matched to the viscosity of the interstitial fluid (24):

$$\frac{k}{k_0} = \frac{\alpha - \alpha^2 + \left(\frac{\theta}{\theta_0}\right)^2}{\alpha \left(\frac{\theta}{\theta_0}\right)^{1/3}} \quad \text{Equation 4}$$

The signals inside and outside the infusion were calculated as the mean pixel value in the distribution volume and an ROI 2.8mm in diameter placed adjacent to the infusion. Noise was estimated as the standard deviation of pixel values in an ROI 2.8mm in diameter placed

in the background. The signal-to-noise ratio (SNR) was calculated by dividing the distribution signal by the noise. The contrast-to-noise ratio (CNR) was calculated by dividing the difference in the signal inside and outside the infusion by the noise.

Statistics

Correlations between parameters were calculated using Pearson's correlation coefficient. Significant differences between groups was measured using Student's t-test with $p < 0.05$ considered significant.

RESULTS

The infusate was readily detectable as a hyperintense region in both the 7T T2-FSE and the T2*-weighted GRE images (Fig. 1). The distribution volume grew in size and became more hyperintense throughout the infusion. Delineating the distribution volume was facilitated by the high image quality; the SNR of the infused region was 24.7 ± 0.7 and the CNR relative to the surrounding brain tissue was 11.2 ± 2.0 .

The DTI images showed that the infusion increased ADC and decreased FA. The ADC increased significantly by a factor of almost three-fold, corresponding to a significant 40% decrease in tortuosity (Table 1, Fig. 2, Fig. 3, Eq. [1]). Before infusion, the diffusion was 150% more restricted than free water. After infusion, the tissue was only 50% more restricted (Fig. 3c). Temporal analysis of ROIs farther from the cannula tip showed a temporal lag corresponding to the time for the distribution to encompass the ROI (Fig. 3d). However, after the lag the ADC increased at a similar rate regardless of position with respect to the infusion source.

The infusion consistently reduced the FA significantly by almost 50% (Table 1, Fig. 3b). Even FA over 7-fold (0.52) the free fluid in the ventricles (0.07 ± 0.02) was reduced to only double the free fluid. The FA was highly correlated to the tortuosity ($R^2 = 0.73$). The initial FA varied widely because of the heterogeneity of the underlying tissue, which included both gray and white matter. Over the entire infusion volume the ADC increased significantly by $115\% \pm 45\%$ and the FA decreased significantly by $46\% \pm 12\%$.

The T2-FSE images showed that the distribution volume scaled linearly with the infusion volume at a V_d/V_i ratio of 2.33 ± 0.53 across all timepoints and infusions ($R^2 = 0.88$, Fig. 4b). The 110% increase in porosity from 20% to $42\% \pm 7\%$ was consistent with the 115% increase in the average ADC of the infusion volume. The Kozeny-Carman relation predicts an increase in the hydraulic conductivity of about 18-fold for this increase in porosity (Eq. [2]), corresponding to porous expansion being restricted to about 20% of the pores (Eq. [4], Fig. 4c).

During the 90-minute recovery period, all parameters trended towards recovery of their baseline values, suggesting the extracellular matrix was recovering its pre-infusion geometry (Table 1). The porosity dropped significantly to $35\% \pm 5\%$. Pixel intensity in the T2-FSE showed a declining trend from $97\% \pm 36\%$ above baseline at the end of the infusion to only $76\% \pm 30\%$ after the recovery period. The T2-FSE signal intensity became more heterogeneous during the recovery period and highlighted specific regions such as the hyperintense white matter pathway indicated in Fig. 1c.

The NHP re-scanned 3 weeks after the first infusion showed no evidence of residually elevated T2-hyperintensity or increased ADC, although the cannula tracks were still detectable on the T2*-GRE images (Fig. 5).

DISCUSSION

This study showed that high-field MRI can be used intra-operatively to measure the distribution and fluid environment of CED infusions. Infused tissue had high contrast in T2-weighted images and DTI images were sensitive to changes in diffusivity and anisotropy caused by the infusion.

The high T2-contrast suggests that co-administration of gadolinium may not be necessary with the transition to higher field strengths. However, T2-hyperintensity may not be an appropriate measure of CED distribution in patients showing pre-infusion hyperintensity due to conditions such as peritumoral edema (7). In such cases, visualizing the distribution may still require T1-weighted imaging of co-infused gadolinium (26–29). The high CNR and image quality of the T2-FSE relative to previous CED studies(6,25) demonstrated the utility of high-field MRI for interrogating the internal spatial heterogeneity of the infusate distribution.

While it is generally accepted that CED achieves large distribution volumes by displacing the interstitial fluid in the extracellular space, it has not been previously established whether changes in the geometry of the porous matrix of the brain facilitate the distribution. The T2-weighted and DTI images in this study both suggested CED expanded the extracellular space. The volume measured in the T2-weighted images indicated that the average porosity after infusion was 42%, an increase of 110% over the 20% baseline state reported in the literature (20–23). Similarly, the DTI data indicated a 115% average increase in ADC in the distribution volume. The decreases in FA and tortuosity were also consistent with extracellular space expansion. The finding that CED increases the extracellular space is consistent with observations from several previous studies, including the mass effect around large-volume CED (30), the capability to distribute particles much larger than the gap sizes of the extracellular space (26,31,32) and the observation that cell swelling from cerebral ischemia negatively effects drug distribution (33). A recent paper found that T2-MRI significantly underestimates the volume of CED compared to autoradiography (25), suggesting the porous expansion may be even larger than suggested in this study.

Further, this study suggested that the expansion of extracellular space was restricted to only about 20% of the pores (Fig. 4c). Each opening pathway would therefore open about 5-fold. This concept is consistent with previous studies showing preferential opening of the perivascular spaces (34), and could explain how CED effectively distributes particles that are larger than measured extracellular spaces in the brain. Ex-vivo electron microscopy of fixed adult brain tissue (22,23) and in-vivo optical imaging (35) have shown that extracellular spaces are about 10 to 65nm wide (35). Despite these small spaces, numerous studies have shown effective CED infusions with particles including gadolinium-loaded liposomes about 125nm wide (26,32) and large adeno-associated viral vectors (31). These studies have consistently demonstrated that the therapeutic distributions achieved by CED closely match the distribution of the carrier fluid (26,29,31,36). The distribution of large particles was not investigated in this study, but is an important issue and should be examined in future research.

An expansion in extracellular space has several important implications for CED. This expansion should be incorporated into theoretical models of CED, which commonly assume a rigid porous matrix (8,37–39). Further, restriction of the extracellular space due to ischemia at low blood pressures may explain the poor distribution of therapeutic agents previously attributed to arterial pulsation (34). The expansion of extracellular space suggests that optimizing CED to achieve maximal drug distribution will require investigating the effect of infusion parameters (e.g. rate, volume) and anatomy (e.g. tumor vs. normal

parenchyma) on the geometry of the extracellular matrix. It would be informative to monitor the ADC beyond the 3-hour data acquisition window in this study to establish the therapeutic window for enhanced drug distribution and the safety of CED. The follow-up data in this study showed that by 3-weeks after the infusion there was no sign of residual infusate, edema or swelling (Fig. 5).

This study identifies high-field DTI as a promising tool for optimizing extracellular space expansion by CED on a patient-by-patient basis. Measuring ADC has significant advantages over using anatomical T1- or T2-weighted images; it eliminates the influence of relaxation differences between the infusate and interstitial fluid, enables direct calculation of the restriction to fluid distribution in the pathway for drug delivery (the tortuosity), eliminates the need for tracer agents and permits direct pixel measurements without whole-brain calculations. This study demonstrated the potential to use 7T MRI, however the high field strength does introduce additional technical challenges for image acquisition (e.g. high specific-absorption rate), image processing (e.g. to correct the large image distortions) and intraoperative imaging (e.g. large fringe fields affecting the infusion pumps). A detailed comparison of 1.5T, 3T and 7T MRI should be conducted prior to implementing intra-operative ADC-tracking clinically. An intra-individual study comparing the effects of field inhomogeneities and the appearance of non-enhanced to contrast-enhanced imaging between and within field strengths would be highly informative. For example, the benefit of higher resolution at 7T for locating the cannula during interventional procedures may be outweighed by the larger image distortions.

There are several potential weaknesses of the methods used in this study that should be acknowledged. This analysis assumed that all infusate distribution occurs through the tortuous extracellular space and ignored intracellular-extracellular exchange, intracellular MR signal components and infusate clearance from the brain. However, these assumptions would have only led this study to underestimate rather than overestimate the results and modeling these factors would have required extrapolation of parameters poorly defined in the literature. Further, the hydraulic conductivity calculation used a literature estimate of the baseline porosity that should be employed with careful consideration for confounding factors such as local edema.

Follow-on scientific studies should evaluate the impact of extracellular space expansion on drug delivery and theoretical models of CED. The impact on drug delivery could be characterized in-vivo by comparing the extracellular space expansion to the distribution of liposomes co-loaded with drug and Gadolinium or ex-vivo with histopathology using a fluorescent label. It would be especially interesting to relate the size of the drug and extracellular space expansion to the achievable distribution. Incorporating this information into theoretical models of CED may improve the accuracy of simulations used to plan patient infusions.

In conclusion, this study showed that high-field MRI can be used intra-operatively to monitor CED. The T2-weighted and DTI images suggested CED expanded the extracellular space. This results and methodologies developed in this study could be used to improve the delivery of therapeutic agents in clinical trials under development for neurodegenerative disease treatment and oncology, as well as for identifying the therapeutic window for enhanced distribution of molecules and informing safety criteria for CED.

Acknowledgments

Grant Support:

This work was supported by grant PO1 CA118816 from the National Institutes of Health.

REFERENCES

1. Bobo RH, Laske DW, Akbasak A, Morrison PF, Dedrick RL, Oldfield EH. Convection-enhanced delivery of macromolecules in the brain. *Proc Natl Acad Sci U S A*. 1994; 91:2076–2080. [PubMed: 8134351]
2. Kunwar S, Prados MD, Chang SM, et al. Direct intracerebral delivery of cintredekin besudotox (IL13-PE38QQR) in recurrent malignant glioma: a report by the Cintredekin Besudotox Intraparenchymal Study Group. *J Clin Oncol*. 2007; 25(7):837–844. [PubMed: 17327604]
3. Gill SS, Patel NK, Hottton GR, et al. Direct brain infusion of glial cell line-derived neurotrophic factor in Parkinson disease. *Nat Med*. 2003; 9(5):589–595. [PubMed: 12669033]
4. Lang AE, Gill S, Patel NK, et al. Randomized controlled trial of intraputamenal glial cell line-derived neurotrophic factor infusion in Parkinson disease. *Ann Neurol*. 2006; 59(3):459–466. [PubMed: 16429411]
5. Marks WJ, Ostrem JL, Verhagen L, et al. Safety and tolerability of intraputamenal delivery of CERE-120 (adeno-associated virus serotype 2-neurturin) to patients with idiopathic Parkinson's disease: an open-label, phase I trial. *Lancet Neurol*. 2008; 7(5):400–408. [PubMed: 18387850]
6. Richardson RM, Gimenez F, Salegio EA, et al. T2 imaging in monitoring of intraparenchymal real-time convection-enhanced delivery. *Neurosurgery*. 2011; 69(1):154–163. [PubMed: 21430597]
7. Sampson JH, Raghavan R, Provenzale JM, et al. Induction of hyperintense signal on T2-weighted MR images correlates with infusion distribution from intracerebral convection-enhanced delivery of a tumor-targeted cytotoxin. *AJR Am J Roentgenol*. 2007; 188(3):703–709. [PubMed: 17312057]
8. Sampson JH, Raghavan R, Brady ML, et al. Clinical utility of a patient-specific algorithm for simulating intracerebral drug infusions. *Neuro-oncology*. 2007; 9(3):343–353. [PubMed: 17435179]
9. Raghavan R, Mikaelian S, Brady M, Chen ZJ. Fluid infusions from catheters into elastic tissue: I. Azimuthally symmetric backflow in homogeneous media. *Phys Med Biol*. 2010; 55(1):281–304. [PubMed: 20009198]
10. Raghavan R, Brady ML, Rodriguez-Ponce MI, Hartlep A, Pedain C, Sampson JH. Convection-enhanced delivery of therapeutics for brain disease, and its optimization. *Neurosurg Focus*. 2006; 20(4):E12. [PubMed: 16709017]
11. Mukherjee P. Development and initial evaluation of 7-T q-ball imaging of the human brain. *Magn Reson Imaging*. 2008; 26(2):171–180. [PubMed: 17692489]
12. Bankiewicz KS, Eberling JL, Kohutnicka M, et al. Convection-enhanced delivery of AAV vector in parkinsonian monkeys; in vivo detection of gene expression and restoration of dopaminergic function using pro-drug approach. *Exp Neurol*. 2000; 164(1):2–14. [PubMed: 10877910]
13. Krauze MT, Saito R, Noble C, et al. Reflux-free cannula for convection-enhanced high-speed delivery of therapeutic agents. *J Neurosurg*. 2005; 103(5):923–929. [PubMed: 16304999]
14. Nicholson C. Diffusion from an injected volume of a substance in brain tissue with arbitrary volume fraction and tortuosity. *Brain Res*. 1985; 333(2):325–329. [PubMed: 3995298]
15. Nicholson C, Phillips JM. Ion diffusion modified by tortuosity and volume fraction in the extracellular microenvironment of the rat cerebellum. *J Physiol*. 1981; 321:225–257. [PubMed: 7338810]
16. Szafer A, Zhong J, Gore JC. Theoretical model for water diffusion in tissues. *Magn Reson Med*. 1995; 33(5):697–712. [PubMed: 7596275]
17. Syková E. Extrasynaptic volume transmission and diffusion parameters of the extracellular space. *Neuroscience*. 2004; 129(4):861–876. [PubMed: 15561404]
18. Carman PC. Fluid flow through granular beds. *Transactions of the Institution of Chemical Engineers*. 1937; 15:150–166.
19. Charras GT, Yarrow JC, Horton MA, Mahadevan L, Mitchison TJ. Non-equilibration of hydrostatic pressure in blebbing cells. *Nature*. 2005; 435(7040):365–369. [PubMed: 15902261]
20. Nicholson C, Sykova E. Extracellular space structure revealed by diffusion analysis. *Trends Neurosci*. 1998; 21(5):207–215. [PubMed: 9610885]
21. Quirk JD, Bretthorst GL, Duong TQ, et al. Equilibrium water exchange between the intra- and extracellular spaces of mammalian brain. *Magn Reson Med*. 2003; 50(3):493–499. [PubMed: 12939756]

22. Kreis TE, Geiger B, Schlessinger J. Mobility of microinjected rhodamine actin within living chicken gizzard cells determined by fluorescence photobleaching recovery. *Cell*. 1982; 29(3):835–845. [PubMed: 6891291]
23. Mastro AM, Babich MA, Taylor WD, Keith AD. Diffusion of a small molecule in the cytoplasm of mammalian cells. *Proc Natl Acad Sci U S A*. 1984; 81(11):3414–3418. [PubMed: 6328515]
24. Brydon HL, Hayward R, Harkness W, Bayston R. Physical properties of cerebrospinal fluid of relevance to shunt function. 1: The effect of protein upon CSF viscosity. *Br J Neurosurg*. 1995; 9(5):639–644. [PubMed: 8561936]
25. Iyer RR, Butman JA, Walbridge S, Gai ND, Heiss JD, Lonser RR. Tracking accuracy of T2- and diffusion-weighted magnetic resonance imaging for infusate distribution by convection-enhanced delivery. *J Neurosurg*. 2011; 115(3):474–480. [PubMed: 21663409]
26. Saito R, Krauze MT, Bringas JR, et al. Gadolinium-loaded liposomes allow for real-time magnetic resonance imaging of convection-enhanced delivery in the primate brain. *Exp Neurol*. 2005; 196(2):381–389. [PubMed: 16197944]
27. Lonser RR, Walbridge S, Murray GJ, et al. Convection perfusion of glucocerebrosidase for neuropathic Gaucher's disease. *Ann Neurol*. 2005; 57(4):542–548. [PubMed: 15786474]
28. Sampson JH, Brady M, Raghavan R, et al. Colocalization of gadolinium-diethylene triamine pentaacetic Acid with high-molecular-weight molecules after intracerebral convection-enhanced delivery in humans. *Neurosurgery*. 2011; 69(3):668–676. [PubMed: 21430586]
29. Su X, Kells AP, Aguilar Salegio EA, et al. Real-time MR imaging with Gadoteridol predicts distribution of transgenes after convection-enhanced delivery of AAV2 vectors. *Mol Ther*. 2010; 18(8):1490–1495. [PubMed: 20551915]
30. Valles F, Fiandaca MS, Bringas J, et al. Anatomic compression caused by high-volume convection-enhanced delivery to the brain. *Neurosurgery*. 2009; 65(3):579–585. discussion 585-576. [PubMed: 19687704]
31. Fiandaca MS, Varenika V, Eberling J, et al. Real-time MR imaging of adeno-associated viral vector delivery to the primate brain. *Neuroimage*. 2009; 47(Suppl 2):T27–T35. [PubMed: 19095069]
32. Gimenez F, Krauze MT, Valles F, et al. Image-guided convection-enhanced delivery of GDNF protein into monkey putamen. *Neuroimage*. 2011; 54(Suppl 1):S189–S195. [PubMed: 20080195]
33. Haar PJ, Broaddus WC, Chen ZJ, Fatouros PP, Gillies GT, Corwin FD. Quantification of convection-enhanced delivery to the ischemic brain. *Physiol Meas*. 2010; 31(9):1075–1089. [PubMed: 20651424]
34. Hadaczek P, Yamashita Y, Mirek H, et al. The "perivascular pump" driven by arterial pulsation is a powerful mechanism for the distribution of therapeutic molecules within the brain. *Mol Ther*. 2006; 14(1):69–78. [PubMed: 16650807]
35. Thorne RG, Nicholson C. In vivo diffusion analysis with quantum dots and dextrans predicts the width of brain extracellular space. *Proc Natl Acad Sci U S A*. 2006; 103(14):5567–5572. [PubMed: 16567637]
36. Richardson RM, Kells AP, Rosenbluth KH, et al. Interventional MRI-guided Putaminal Delivery of AAV2-GDNF for a Planned Clinical Trial in Parkinson's Disease. *Mol Ther*. 2011; 19(6):1048–1057. [PubMed: 21343917]
37. Morrison PF, Laske DW, Bobo H, Oldfield EH, Dedrick RL. High-flow microinfusion: tissue penetration and pharmacodynamics. *Am J Physiol*. 1994; 266(1 Pt 2):R292–R305. [PubMed: 8304553]
38. Rosenberg GA, Kyner WT, Estrada E. Bulk flow of brain interstitial fluid under normal and hyperosmolar conditions. *Am J Physiol*. 1980; 238(1):F42–F49. [PubMed: 7356021]
39. Baxter LT, Jain RK. Transport of fluid and macromolecules in tumors. I. Role of interstitial pressure and convection. *Microvasc Res*. 1989; 37(1):77–104. [PubMed: 2646512]

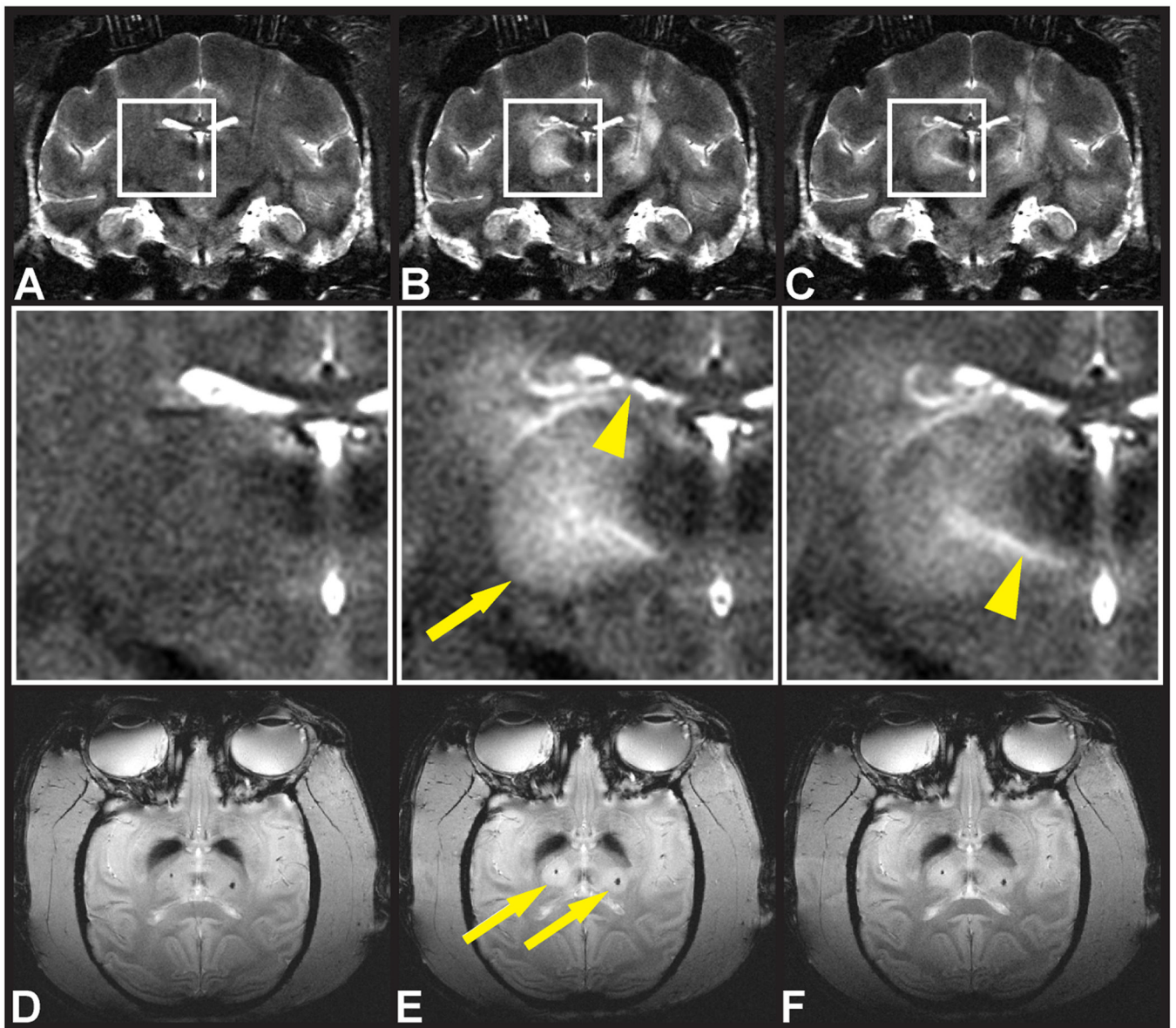


Fig. 1. High-resolution intra-operative FSE and GRE images showed the distribution of infusate T2-FSE acquired (A) before, (B) immediately after and (C) 90 minutes after an infusion. (D-F) GRE acquired at the same timepoints. Arrows indicate the infusion volumes. Arrowheads point to ventricular compression (B, inset) and heterogeneity observed during clearance of the infusate (C, inset). The hypointense foci in the GRE are susceptibility effects of the infusion cannulae.

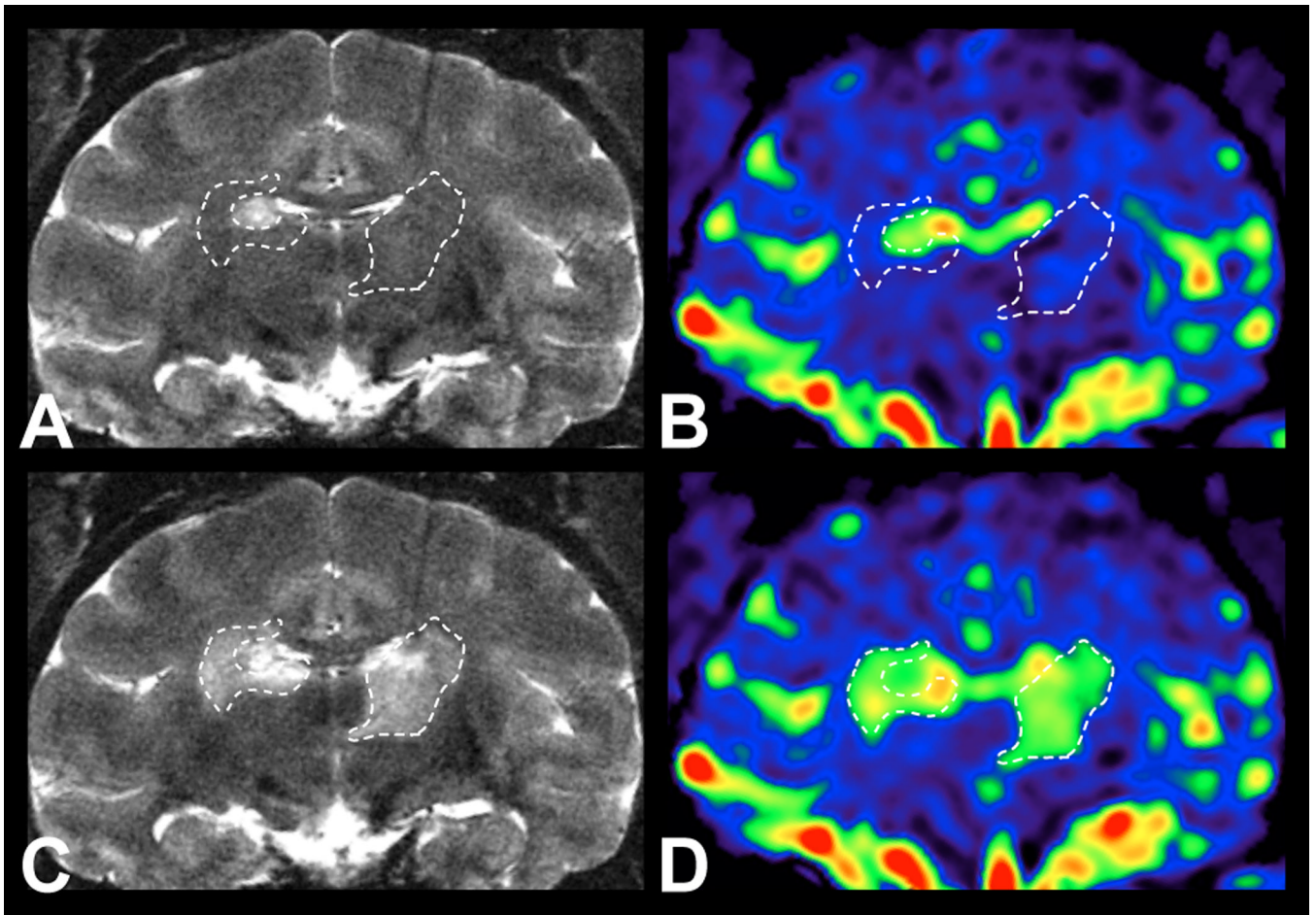


Fig. 2. Diffusivity increased in the infused tissue

(A) T2-FSE and (B) DTI ADC map acquired prior to and (C-D) after bilateral infusions. The ADC increased dramatically in the regions of elevated T2-hyperintensity (dotted lines).

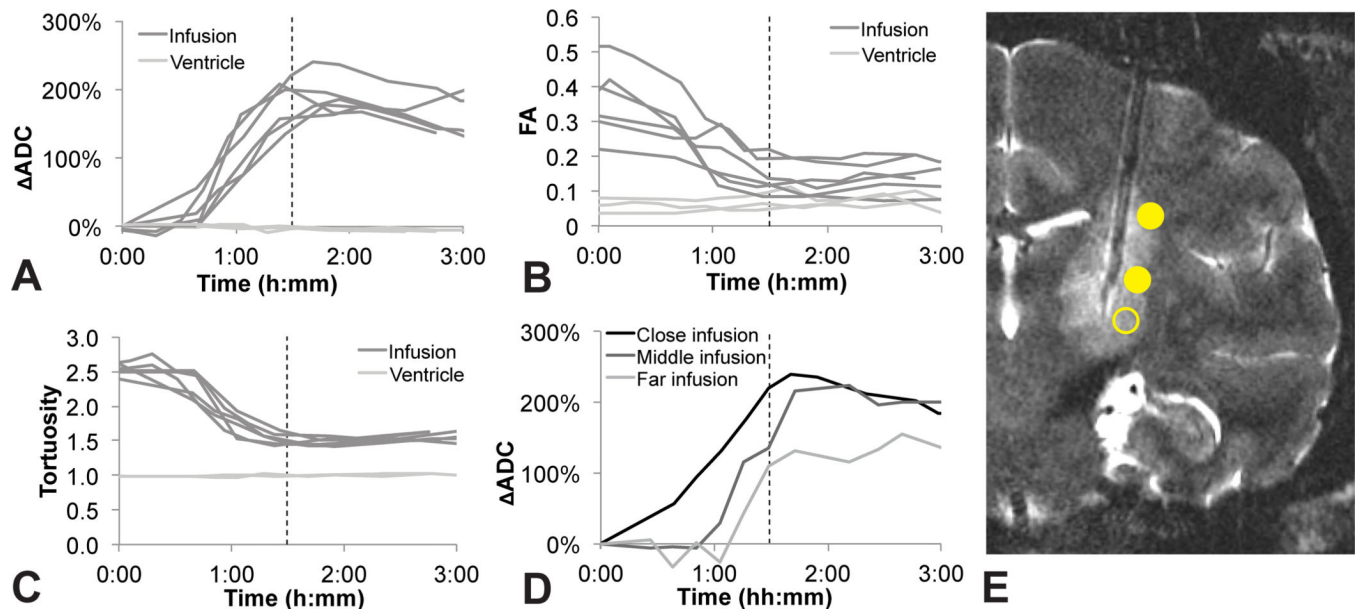


Fig. 3. Temporal analysis of serial intra-operative MRI data

Dashed lines indicate the end of the 90-minute infusion and the start of the 90-minute recovery. (A) ADC increased, (B) FA decreased and (C) tortuosity decreased during the infusion. (D) ROIs farther from the cannula tip lagged temporally lagged the closer ROIs, but increased at approximately the same rate. (E) T2-FSE showing the placement of ROIs lateral to the cannula tip (solid ROI, all panels) and farther from the tip (dashed ROIs, panel D). The close, middle and far ROIs were placed 2mm, 5mm and 10mm from the cannula tip.

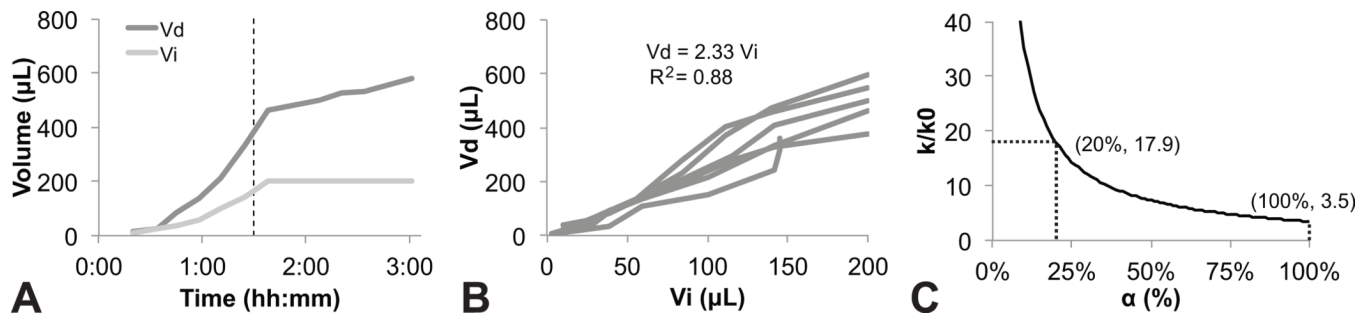


Fig. 4. Analysis of the Vd/Vi ratio and estimation of selective pore expansion

(A) Temporal plot of a sample 200 μL infusion. (B) The distribution volume (Vd) scaled at 2.33 times the infusion volume (Vi). (C) Selectively opening 20% of the pathways would achieve the predicted 17.9-fold increase in hydraulic conductivity (Eq. [4]). Opening all pathways is predicted to only increase the hydraulic conductivity 3.5-fold.

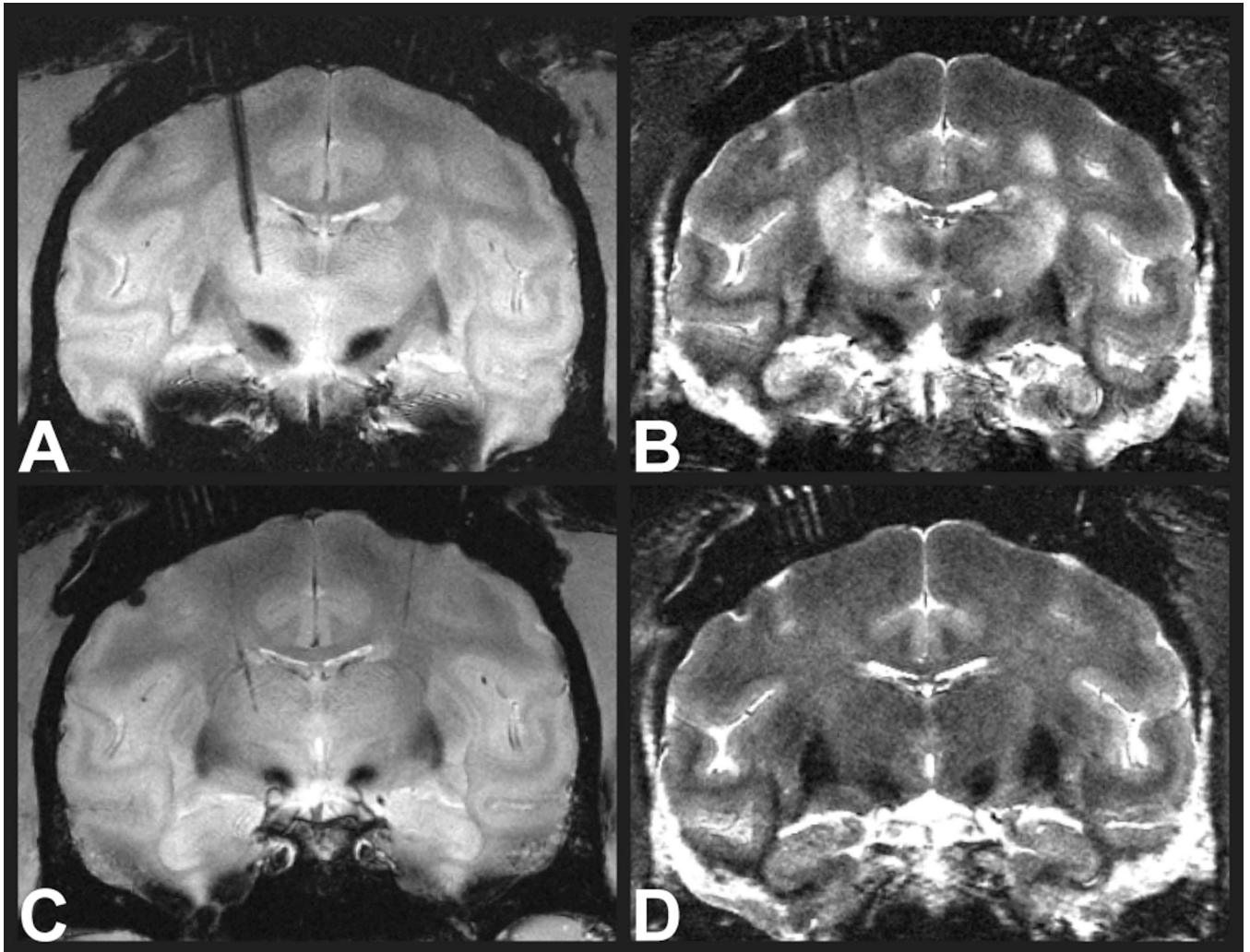


Fig. 5. Post-infusion recovery at three weeks

(A) T2*-GRE and (B) T2-FSE acquired at the end of an infusion. (C) T2*-GRE and (D) T2-FSE acquired three weeks later. There was no residual evidence of infusate or hyperintense edema in the T2-FSE but the cannula tract was still detectable in the T2*-GRE.

Table 1

Parameter	Before infusion	After infusion	After recovery
Change in Apparent Diffusion Coefficient (Δ ADC)	0% \pm 0%	185% \pm 27% *	115% \pm 69%
Fractional Anisotropy (FA)	0.32 \pm 0.11	0.17 \pm 0.09 *	0.15 \pm 0.05
Tortuosity (τ)	2.51 \pm 0.08	1.49 \pm 0.06 *	1.62 \pm 0.15
Porosity (θ)	20% ^a	42% \pm 7% *	35% \pm 5% **

^aFrom literature;

* Significant change from before infusion (p<0.05);

** Significant change from end of infusion (p<0.05)